small methods
www.small-methods.com

Nanofibers Comprising Interconnected Chain-Like Hollow N-Doped C Nanocages as 3D Free-Standing Cathodes for Li–S Batteries with Super-High Sulfur Content and Lean Electrolyte/Sulfur Ratio

*Rakesh Saroha and Jung Sang Cho**

The development of a suitable cathode host that withstands high sulfur content/loading and low electrolyte/sulfur (E/S) ratio is particularly important for practically sustainable Li–S batteries. Herein, a facile approach is utilized to prepare free-standing 3D cathode substrates comprising nitrogen-doped carbon (N-C) scaffold and metal–organic framework derived interconnected chain-like hollow N-C nanocages, forming a highly porous N-C nanofiber (HP-N-CNF) framework. The N-C skeleton provides highly conductive pathways for fast lithium ion/electron diffusion. The hollow interconnected N-C nanocages not only offer enough space to absorb a high volume of active material but also effectively channelize severe volume stress during the electrochemical performance. The Li–S cell utilizing HP-N-CNF as cathode host displays exceptional battery parameters with high effective sulfur content (83.2 wt%), ultrahigh sulfur loading (14.3 mg cm^{-2}), and low E/S ratio (6.8 µL mg^{-1}). The Li–S cell exhibits a maximum areal capacity of 12.2 mAh cm^{-2} which stabilizes at ≈5.5 mAh cm^{-2} after the 130th cycle at 0.05 C-rate and is well above the theoretical threshold. Therefore, the proposed unique nanostructure synthesis approach would open new frontiers for developing more realistic and sustainable host materials with feasible battery parameters for various energy storage applications.

1. Introduction

The tremendous advances in Li–S batteries (LSBs) during the last decade have brought them to the forefront of several rechargeable battery technologies.[1–10] However, the commercialization of LSBs is still lagging compared to their counterparts owing to several fundamental drawbacks such as the highly insulating nature of sulfur and its discharge product, i.e., Li_2S formation and migration of lithium polysulfide (LiPS) species, which results in the loss of active material, severe volume changes during charge–discharge, and poor cycling stability accompanied by low Coulombic efficiencies.[11–17] In addition, highly impractical cell parameters, such as low effective sulfur content in the electrode (<70 wt%), low sulfur loading (<2 mg cm^{-2}), and high electrolyte/sulfur (E/S) ratio (>10 µL mg^{-1}) generally result in overrated electrochemical performance such as high initial discharge capacities approaching the theoretical value, exceptional rate capabilities, and outstanding cycling stabilities.[13,18–23]

To explore the more practical aspects of LSBs, researchers worldwide are now focusing on developing an advanced cathode substrate as a host material to accommodate a high effective sulfur content (70–75 wt%) along with an ultrahigh active material loading.[18–20,23–27] The typical process of coating an active material slurry on an aluminum current collector has limitations because of the density difference between sulfur and its discharge product.[3] Owing to the large volume variation between sulfur and Li_2S during the redox process, crack formation or pulverization of the electrodes is highly evident in conventional electrodes, which is even more pronounced in the case of high-sulfur content or high-sulfur loading electrodes.[1] Additionally, the corrosion of metal current collector such as aluminum or stainless steel affects the functioning of LSBs employing highly concentrated polysulfides as active material.[20] Thus, it is highly desirable that the host material be a free-standing 3D substrate that can also be applied as a current collector and possess sufficient porosity to withstand the volume stress developed during cycling for LSBs with viable parameters. The porous structure allows the consumption of a low electrolyte volume with efficient percolation to the lowest level of the 3D substrate, thus permitting high active material utilization during the electrochemical process. Among the various available 3D current collectors that have been employed as cathode substrates in LSBs, polyacrylonitrile (PAN)-based nitrogen-doped carbon nanofibers (N-CNFs) have been studied extensively owing to their ease of synthesis.[28–30] For example, Yao et al. prepared a 3D free-standing N-CNF membrane through an electrospinning technique followed by

R. Saroha, J. S. Cho
Department of Engineering Chemistry
Chungbuk National University
1, Chungdae-Ro, Seowon-Gu, Cheongju-Si
Chungbuk 361-763, Republic of Korea
E-mail: jscho@cbnu.ac.kr

The ORCID identification number(s) for the author(s) of this article can be found under https://doi.org/10.1002/smtd.202200049.

DOI: 10.1002/smtd.202200049

carbonization and employed it as the LSB cathode substrate.[28] Similarly, Guo et al. synthesized and tested N-CNF electrodes for Li-LiPSs battery performance.[29] However, the absence of a high surface area and pore volume did not allow for high loading or sulfur content in the above studies, which limits their practical applicability.

Highly porous advanced carbon nanomaterials as 3D cathode substrates are generally visualized by controlling the pore formation process inside the host to effectively encapsulate the sulfur species.[31–33] In this regard, metal–organic frameworks (MOFs) play a vital role as self-sacrificing agents for the development of highly ordered mesopores inside carbon nanostructures. In particular, a Zn-based zeolitic imidazole framework (ZIF-8, a class of MOFs) was reported as a self-sacrificing template to develop porous interlayer materials owing to the volatile nature of the central Zn atom.[3] Other studies have also reported the synthesis of 1D porous carbon nanostructures using the conventional electrospinning method and MOFs. For example, MOF-derived porous CNFs, including interconnected bimodal pores have been applied to Li–Se battery applications.[34] However, a multistep synthesis approach to obtain the final product complicates the entire process. Therefore, based on the above discussion, we performed a facile one-pot synthesis of 1D nanostructured highly porous nitrogen-doped carbon nanofibers to form a 3D free-standing cathode substrate that simultaneously behaves as a current collector for advanced LSBs with practical cell parameters.

The 3D structured highly porous nitrogen-doped carbon nanofiber (HP-N-CNF) cathode substrate was prepared simply via a combination of typical electrospinning technique followed by the carbonization process of the as-spun PAN/ZIF-8 composite nanofibers. During the carbonization process at a high temperature, the ultrafine ZIF-8 polyhedra are broken down into volatile zinc metal and organic linkers, which resemble hollow carbon nanocages that eventually form interconnected chain-like highly ordered mesopores along the fiber length. In addition, the decomposition of the PAN resulted in the formation of a highly conductive nitrogen-doped carbon (N-C) matrix. The highly conductive N-C framework provides enormous channels for fast ionic and electronic transport, whereas the numerous ordered mesopores allow efficient impregnation of the active material along with high loading. The porous structure also channels off the undesired volume variation stress during repeated cycling. Besides, the well-developed hollow nanocages effectively acts as reservoirs for efficient electrolyte immersion which is vital for uniform dispersion and high active sulfur utilization especially for low E/S ratio arrangement. This facile synthesis approach of such a controlled porous fibrous morphology with highly uniform and densely packed nanocages with open voids as reservoirs which resembles a chain-like structure has been introduced for LSBs in this study. The advanced LSBs were then visualized using a 3D structured HP-N-CNF cathode substrate impregnated with a high molar (5.7 M) active sulfur material in the form of a polysulfide catholyte (Li_2S_6; 0.95 M) solution. The typical assembled LSBs comprised ultrahigh effective sulfur content (76.8 wt%), high sulfur loading (4.8 mg cm^{-2}), and low E/S ratio (9.6 µL mg^{-1}). Moreover, the structural merits allowed us to further increase the active material loading to 10.0 mg cm^{-2} (77.9 wt%) and 14.3 mg cm^{-2} (83.2 wt%) with a low E/S ratio of 7.4 and 6.8 µL mg^{-1}, respectively. Even with such strident conditions, the Li–S cell employing HP-N-CNF free-standing cathode substrate exhibits a maximum areal capacity of 12.2 mAh cm^{-2} which stabilized to 5.5 mAh cm^{-2} at the end of the 130th cycle at a 0.05 C-rate and is well above the theoretical benchmark of 4.0 mAh cm^{-2} for the presently available commercial $LiCoO_2$ cathode and graphite anode system. We believe that the present strategy of synthesizing highly porous 1D nanostructures with uniformly distributed ordered mesopores could be utilized for developing advanced cathode host substrates for viable metal–sulfur battery technology.

2. Results and Discussion

HP-N-CNFs comprising interconnected chain-like hollow N-C nanocages with open pores were synthesized using an electrospinning technique followed by a facile one-step heat-treatment process. The detailed synthesis mechanism is shown in **Scheme 1**a①–③. The spinning solution containing PAN polymer and ZIF-8 polyhedra (∅ = 100 nm) was electrospun, which subsequently resulted in the PAN nanofibers being uniformly composited with numerous ZIF-8 polyhedra (Scheme 1a①). The obtained PAN/ZIF-8 composite nanofibers were stabilized at 150 °C and subsequently subjected to a one-step carbonization process at 1000 °C for 2 h in a N_2 atmosphere. During high-temperature heat treatment, PAN was carbonized to a N-C framework, whereas the ZIF-8 polyhedra, in which the central zinc atom is connected to the organic linkers (imidazolate units) via N atoms, were disintegrated into the highly volatile Zn/Zn^{2+} metal and interconnected chain-like hollow N-embedded carbonized products (N-C nanocages), as shown in Scheme 1a②. The highly volatile reduced zinc metal evaporates at a high temperature of 1000 °C, thus leaving numerous uniformly distributed ordered mesopores of 50 nm along the fiber length. The detailed mechanism involving structural evolution of ZIF-8 polyhedra to hollow N-C nanocages as a function of temperature is shown in Scheme 1b. As the reaction temperature increases from ambient to 350 °C, the N-rich organic ligands in ZIF-8 polyhedra carbonized to a stable and rigid N-C product as a carbon layer on the surface. With further increase in temperature to 600 °C, the decomposition of ZIF-8 core begins whereas the rigid carbon layer drags polyhedra surface outward. When temperature reaches to 900 °C, the outward shrinkage process intensifies and resulted in the collapse of entire inner core of ZIF-8. At 1000 °C, evaporation of metallic Zn will take place along with the formation of dense carbon shells.[35] The synergistic effects of volatile zinc metal removal and outward contraction mechanism eventually results in hollow N-C nanocages. Besides, the heating also resulted in the longitudinal shrinkage of the nanofiber that allows hollow nanocages to pack closely and form chain-like nanostructure. This facile approach resulted in a highly porous and nitrogen-doped carbon nanofiber skeleton with enormous interconnected conductive channels for rapid lithium-ion transfer and efficient electrolyte percolation when used as the cathode substrate (Scheme 1a③). The HP-N-CNF sheets were then punched into 3D discs (∅ = 14 mm) and used as

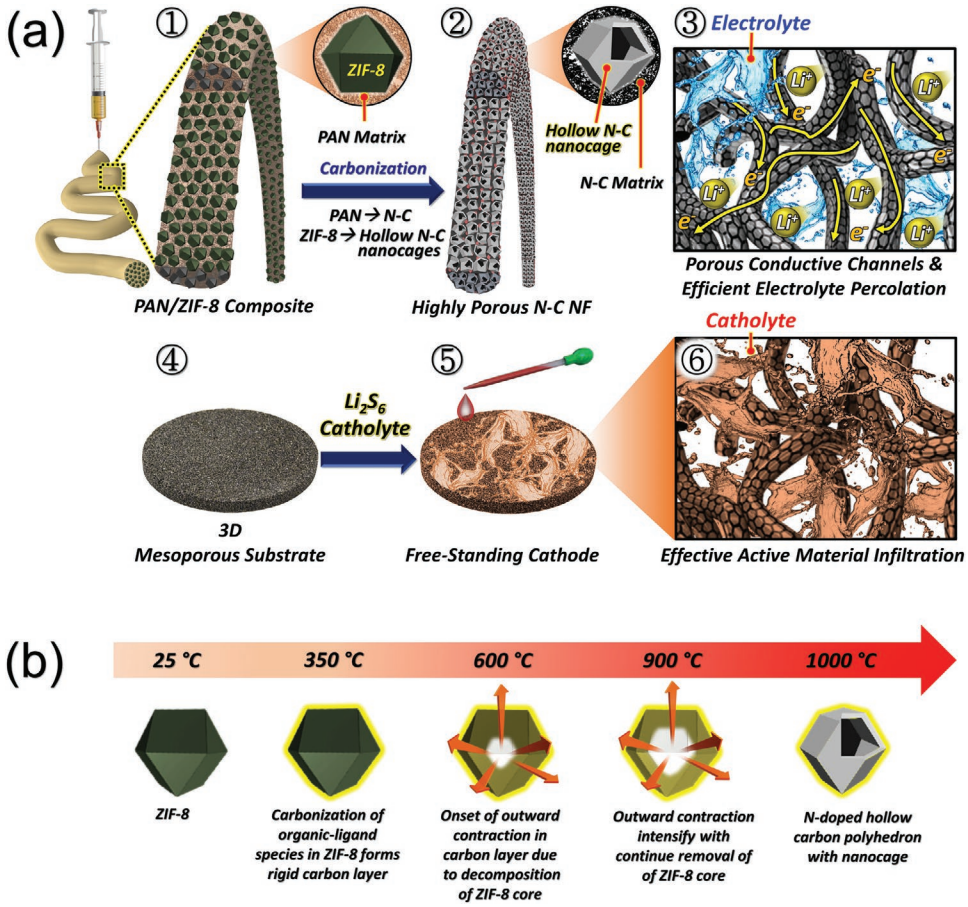

Scheme 1. a) Schematic representation of (①, ②, and ③) formation mechanism of highly porous nitrogen-doped carbon nanofiber comprising interconnected chain-like hollow N-C nanocages with open pores and (④, ⑤, and ⑥) its applicability as a free-standing 3D cathode host for practically viable LSBs and b) detailed mechanism involving structural evolution of ZIF-8 polyhedra to the hollow N-doped carbon nanocages as a function of temperature.

a free-standing mesoporous cathode substrate (Scheme 1a④). The 3D mesoporous substrate was infiltrated with a highly concentrated lithium polysulfide (LiPS) catholyte as a sulfur source to obtain a free-standing cathode (Scheme 1a⑤). The availability of numerous ordered mesopores in the cathode substrate not only absorbs the liquid active material effectively but also provides sufficient space to mitigate the volume variation during the electrochemical processes (Scheme 1a⑥). Therefore, the unique nanostructured synthesis approach simultaneously allows for ultrahigh loading and super-high effective sulfur content in the electrode along with a low electrolyte volume intake, which subsequently resulted in viable LSBs comparable to commercial systems.

To explore the formation mechanism more comprehensively, microstructural and phase analyses of the obtained nanofibers at each synthesis step were performed thoroughly. The field-emission scanning electron microscope (FE-SEM), X-ray diffraction (XRD), and thermogravimetric (TG) analysis results of the stabilized PAN/ZIF-8 composite nanofiber mat are shown in **Figure 1**. The FE-SEM image (Figure 1a) reveals a continuous 1D fibrous morphology with an average diameter of 600 nm. Moreover, the cross-sectional image shown in the inset of Figure 1a clearly indicates that the ZIF-8 polyhedra are well confined and sparsely distributed within the as-spun fiber framework. Furthermore, the rough surface of the nanofiber (Figure 1b) is also evident because of the uniform dispersion of the ZIF-8 polyhedra (size of 100 nm) along the fiber length. The physical characterization results, including the FE-SEM, XRD, and TG curves of the as-prepared ZIF-8 polyhedra are shown in Figure S2a–c in the Supporting Information. Furthermore, the XRD pattern of the stabilized PAN/ZIF-8 composite nanofibers shown in Figure 1c primarily displayed a diffraction pattern similar to the ZIF-8 polyhedra (Figure S2b, Supporting Information) due to the high amount of ZIF-8. The TG analysis curve shown in Figure 1d suggests continuous weight loss in a stepwise manner over different temperature regions. In the low-temperature region (≤350 °C), the crystal water was removed along with the initialization of the carbonization process of PAN. In the mid-temperature region (350–600 °C), the ZIF-8 polyhedra started disintegrating into the highly volatile reduced Zn/Zn^{2+} species and organic linkers, whereas the carbonization process continued concurrently. The organic linkers were ditopic imidazolate units connected to the Zn atoms via N atoms, subsequently converted to the interconnected N-doped carbonized products (hollow N-C nanocages), whereas the highly volatile reduced Zn/Zn^{2+} species begins to vaporize.

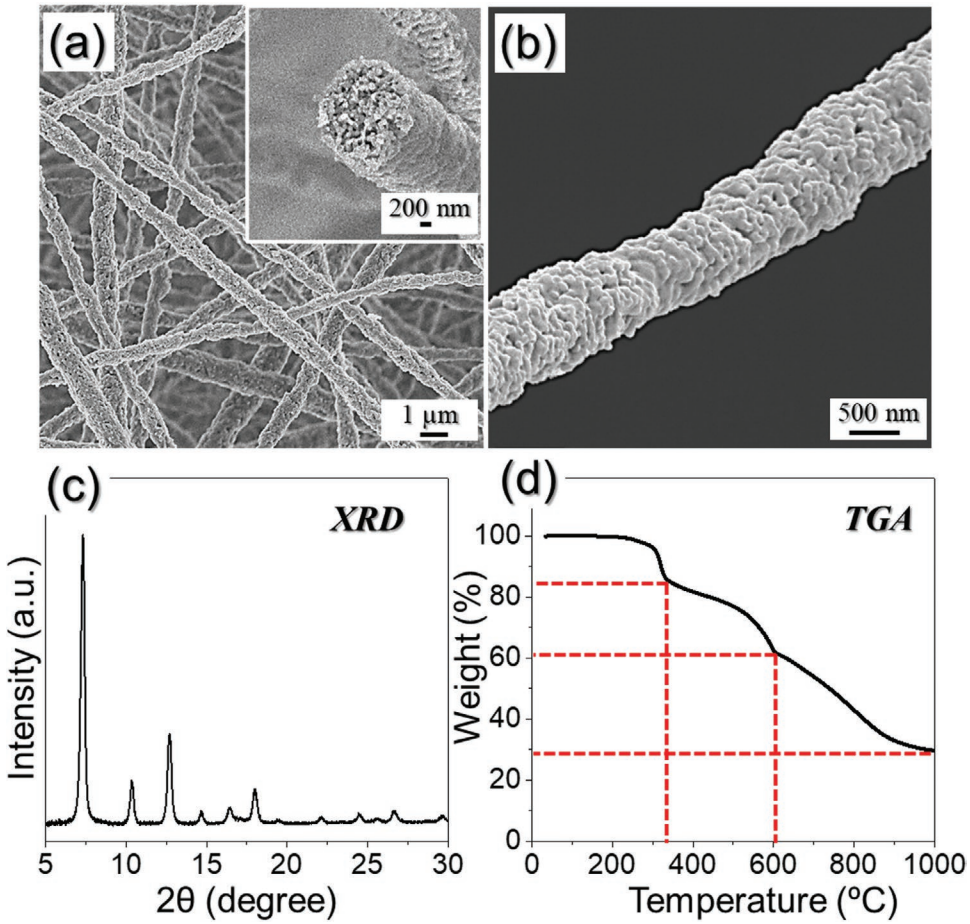

Figure 1. Physical characterizations of as-spun PAN/ZIF-8 composite nanofibers obtained after stabilization at 150 °C overnight: a,b) FE-SEM images, c) XRD pattern, and d) TG curve.

With a further increase in the temperature (600–1000 °C), numerous ZIF-8 polyhedra break down with simultaneous removal of Zn/Zn^{2+} species from the fiber, giving rise to highly ordered mesopores throughout the fiber length (Scheme 1b). The TG curve seems to stabilize near 1000 °C, indicating the removal of the volatile species from the fiber, thus leaving only a highly porous carbon framework that comprises interconnected chain-like hollow N-C nanocages with open pores. Based on the thermogravimetric analysis (TGA) observations, the heat-treatment of the stabilized PAN/ZIF-8 composite nanofiber was carried out at 1000 °C for 2 h in a N_2 environment to form HP-N-CNFs.

The results of physical characterization of HP-N-CNF obtained at 1000 °C are shown in **Figure 2**. The FE-SEM image (Figure 2a) suggests that the 1D fibrous morphology of the composite nanofibers remained intact even after the heat-treatment process and the nanofibers had an average diameter of 500 nm. The high-resolution FE-SEM image shown in Figure 2b clearly suggests the presence of tightly connected highly ordered mesopores (open pores with a diameter of 50 nm) all over the nanofiber surface. The removal of volatile reduced zinc and subsequent shrinkage during the carbonization process at high temperatures resulted in the formation of interconnected chain-like hollow N-C nanocages. In addition, the hollow N-C units were uniformly distributed inside the carbonaceous framework, primarily comprising the N-C matrix only. This observation confirms the homogeneous distribution of the ZIF-8 polyhedra in the as-spun carbon nanofibers, as indicated in Figure 1b. The transmission electron microscopy (TEM) images shown in Figure 2c,d confirm the above results, in which the bright and dark regions correspond to the N-C hollow nanocages and N-doped carbonaceous material, respectively. The high-resolution TEM images (Figure 2e,f) clearly suggest the presence of uniform-sized hollow N-C nanocages (≈50 nm in diameter) surrounded by a carbon shell with a thickness of ≈10 nm. The selected area electron diffraction (SAED) pattern presented in Figure 2g confirms the presence of carbonaceous materials only. The two well-resolved diffraction rings could be assigned to the (002) and (101) planes of the carbon material present in the nanofibers. The XRD pattern (Figure 2h) also showed two broad peaks corresponding to the carbonaceous material without an impurity phase, suggesting that HP-N-CNF was primarily composed of carbon nanomaterial only. The elemental mapping results presented in Figure 2i indicate the presence of carbon, nitrogen, and oxygen along with no traces of zinc metal suggesting complete removal of volatile metal because of high-temperature heating. The oxygen is attributed to the formation of carbon-oxygen bonds during

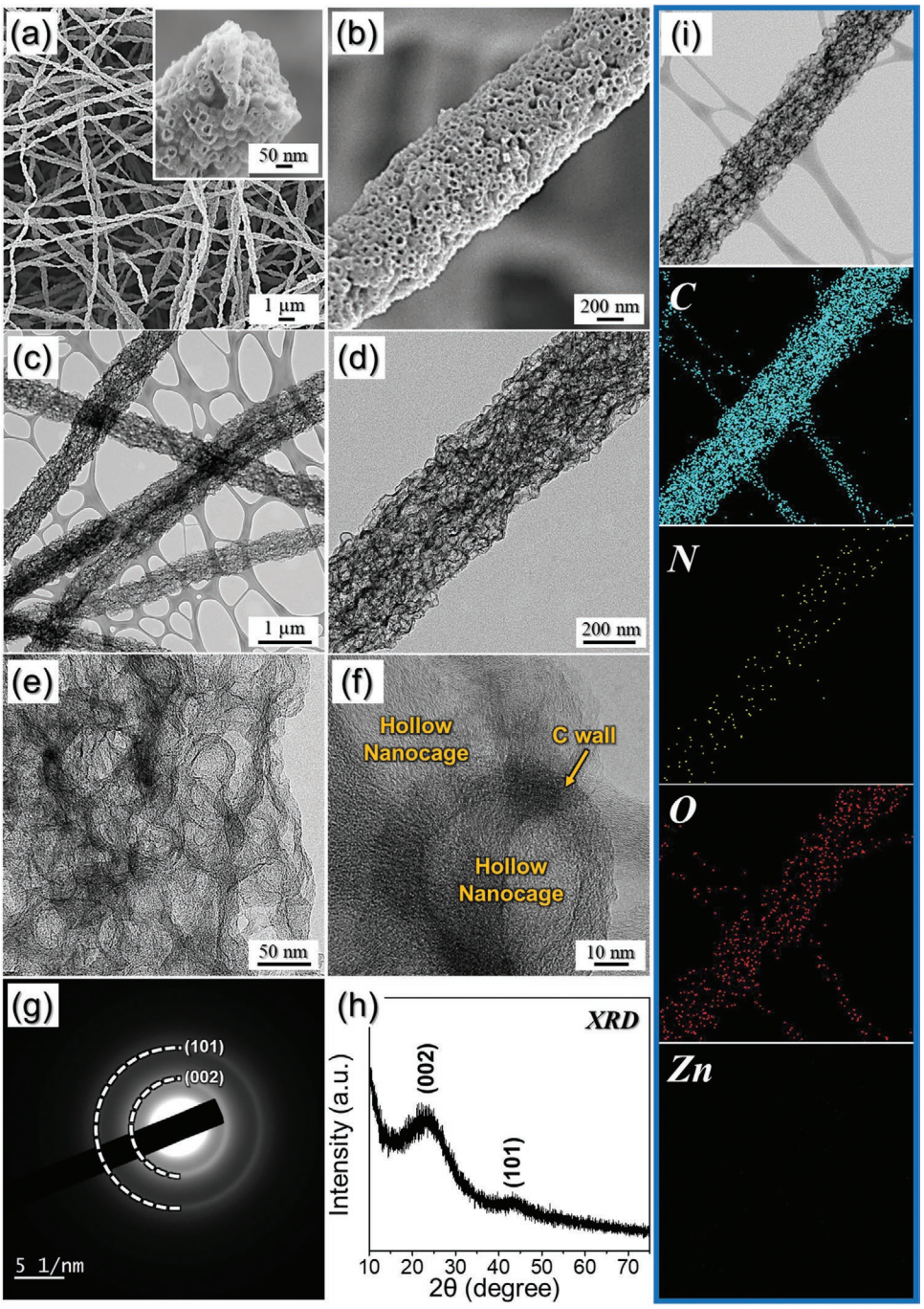

Figure 2. Characterizations of the HP-N-CNF obtained after the heat-treatment of the as-stabilized nanofibers at 1000 °C in a N_2 atmosphere: a,b) FE-SEM images, c,d) TEM images, e,f) HR-TEM images, g) SAED pattern, h) XRD pattern, and i) elemental mapping images.

the stabilization process in air atmosphere. In addition, the nitrogen component in the nanofibers originated from the decomposition of the PAN and ZIF-8 species.

X-ray photoelectron spectroscopy (XPS) analysis was performed to study the various chemical bonding states of the different elements present in HP-N-CNF. The XPS survey spectrum shown in **Figure 3**a indicates the existence of sharp photoelectron signals corresponding to the C 1s, N 1s, and O 1s states in the composite nanofibers. A carbon correction was also employed in the XPS data with respect to the standard binding energy of C 1s (284.8 eV). The high-resolution C 1s XPS profile (Figure 3b) suggests the presence of well-separated peaks at binding energies of 284.8, 286.5, 288.5, and 292.0 eV, which correspond to the C=C, C—N, C—O, and C=O bonds, respectively, in the HP-N-CNF.[5] The strong photoelectron signal for C=C along with C—N suggested the presence of carbonaceous material only along with N doping to form an N-doped carbon skeleton.[36,37] Furthermore, the deconvoluted N 1s XPS profile

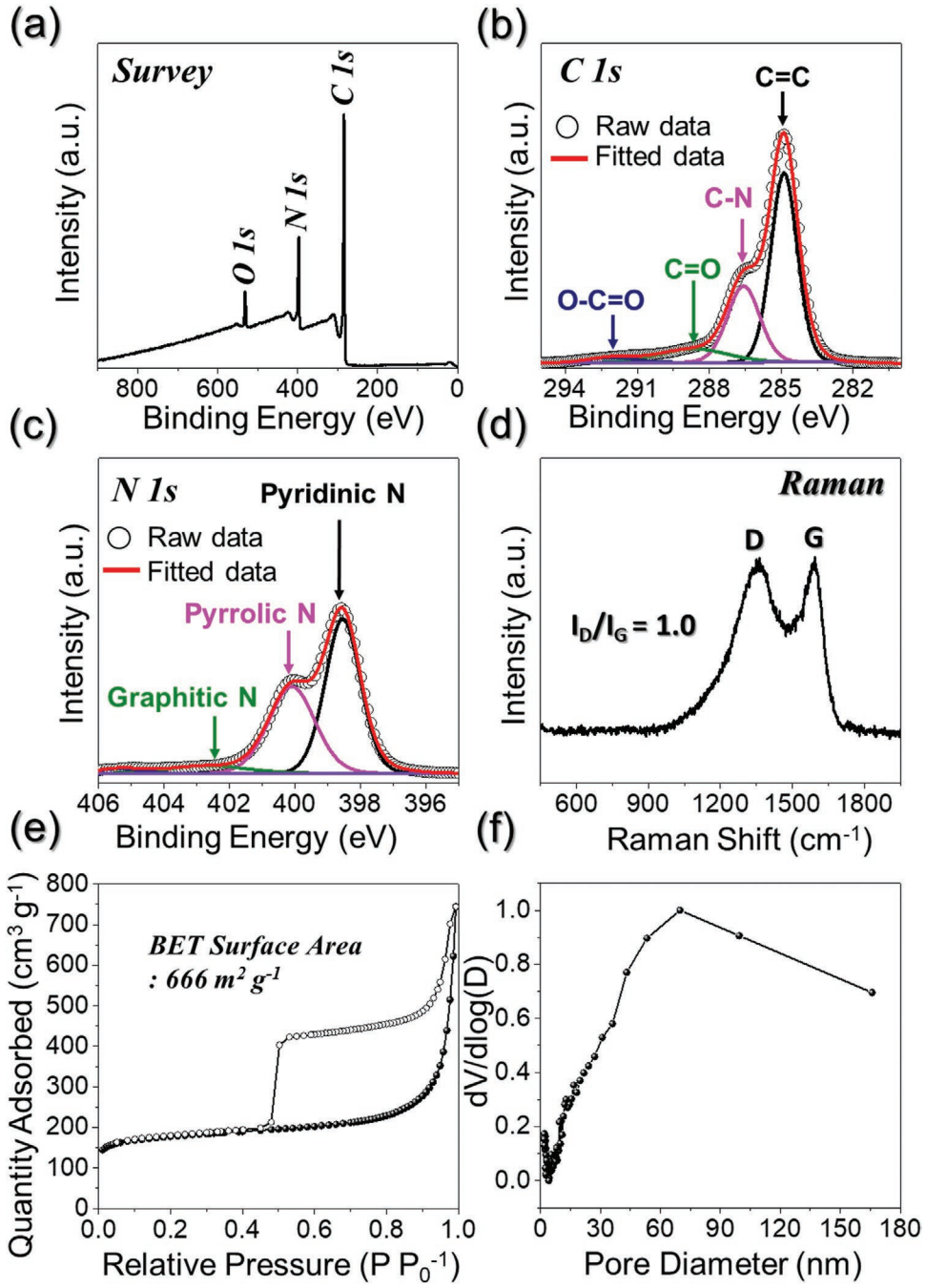

Figure 3. a) XPS survey spectrum, b) deconvoluted C 1s XPS spectrum, c) deconvoluted N 1s XPS spectrum, d) Raman spectrum, e) N_2 adsorption–desorption isotherms, and f) pore size distribution curve of HP-N-CNF.

shown in Figure 3c shows three peaks centered at binding energies of 398.5, 400.1, and 402.8 eV, corresponding to pyridinic-N, pyrrolic-N, and graphitic-N species, respectively, confirming the N doping in the carbon framework again.[37] The elemental analysis (EA) results confirm the above findings, which quantify the nitrogen and carbon content in HP-N-CNF to be 22.3 and 68.5 wt%, respectively, as shown in Table S1 in the Supporting Information. The unusually high N-doping was primarily derived from the decomposition of nitrogen-containing organic groups present in the PAN and the high amount of ZIF-8 polyhedra in the composite nanofibers. Raman spectroscopy was performed to analyze the carbonaceous material structure of HP-N-CNF, as shown in Figure 3d. The Raman spectrum indicates typical signatures of the D-band (1355 cm^{-1}) and G-band (1593 cm^{-1}) with a relative intensity ratio (I_D/I_G) of ≈1.0, suggesting that the carbonaceous material is somewhat fractured, which was derived from the decomposition of PAN matrix and N-rich organic ligands in ZIF-8 polyhedra in the composite nanofibers during the high-temperature heat treatment.[38] The removal of highly volatile reduced Zn/Zn^{2+} metal from the

nanofiber framework also generated numerous interconnected hollow N-C nanocages with sizes in the mesopore range, as discussed above. To validate this, N_2 adsorption–desorption isotherms were investigated using nitrogen as the adsorbate gas via the Brunauer–Emmett–Teller (BET) technique, as shown in Figure 3e. The isotherms indicate a type-IV BET curve, which suggests the high porosity of HP-N-CNF. The surface area of the HP-N-CNFs was 666 m^2 g^{-1} (pore volume: 1.15 cm^3 g^{-1}), which is predominantly attributed to the presence of open pores all over the nanofiber surface, as confirmed by the Barrett–Joyner–Halenda pore size distribution curve (Figure 3f). The peak centered around 70 nm originates from the removal of Zn/Zn^{2+} species from the structure. Overall, the XPS, Raman, and BET curves suggest that HP-N-CNF mainly consists of N-C material with a fractured carbonaceous framework comprising interconnected hollow N-C nanocages with pore sizes in the mesoporous range.

To further elucidate the structural merits of HP-N-CNF, nonporous nitrogen-doped carbon nanofibers (NP-N-CNF), i.e., without ZIF-8 polyhedra, were also prepared. The physical characterization results for the as-spun PAN nanofibers obtained after the two-stage stabilization process (150 °C overnight and then at 200 °C for 1 h in an air atmosphere) are shown in Figure S3a–d in the Supporting Information. The FE-SEM images (Figure S3a,b, Supporting Information) suggest that the stabilized PAN nanofibers display a 1D fibrous morphology with an average diameter of ≈200 nm. Moreover, a smooth fiber surface is also evident (Figure S3b, Supporting Information) as no ZIF-8 polyhedra were present. The XRD shown in Figure S3c in the Supporting Information displays two diffraction peaks at $2\theta = 17°$ and 29°, which matches well with previous reports on PAN precursors.[39–41] Furthermore, the thermal stability of the pristine PAN nanofibers was investigated using TG analysis, as shown in Figure S3d in the Supporting Information. A sudden weight drop started at 300 °C, indicating the onset of the carbonization process. Moreover, a monotonic weight loss up to 1000 °C was also observed, suggesting continued removal of the PAN polymer. In this study, we observed that for temperatures higher than 400 °C, the shrinkage in the free-standing PAN nanofiber mat makes it highly fragile, and thus, there is no free-standing disc. Therefore, a temperature of 400 °C was chosen as the optimum temperature to obtain pristine nonporous N-CNF from the PAN nanofiber mat.

The physical characterization results of the NP-N-CNF obtained after heat treatment of the PAN nanofiber mat are shown in Figure S4 in the Supporting Information. The FE-SEM image shown in Figure S4a in the Supporting Information reveals a dense 1D fibrous morphology with an average diameter of 200 nm. Additionally, the smooth surface of the NP-N-CNF was evident because of the absence of ZIF-8 polyhedra (Figure S4b, Supporting Information). The TEM images in Figure S4c,d in the Supporting Information also confirm the synthesis of highly dense, smooth, and pores-free nanofibers. The high-resolution TEM (HR-TEM) image in Figure S4e in the Supporting Information suggest that the carbonaceous material in NP-N-CNF is primarily composed of amorphous carbon. The SAED pattern shown in the inset of Figure S4e in the Supporting Information also reveals the presence of a diffraction ring corresponding to the (002) plane of the carbonaceous material. Additionally, the presence of the (002) crystal plane in the XRD pattern (Figure S4f, Supporting Information) confirmed these results. The elemental dot mapping results shown in Figure S4g in the Supporting Information indicate the uniform dispersion of carbon and nitrogen elements only. These results suggest that the as-prepared pristine NP-N-CNF is free from pores and only consists of amorphous carbon. The elemental composition and chemical bonding states in pristine NP-N-CNF were further validated using XPS analysis, as shown in Figure S5a,b in the Supporting Information. The XPS survey spectra (Figure S5a, Supporting Information) indicate the presence of photoelectron signals that primarily correspond to the C 1s and O 1s states. However, small traces of the N 1s signal are also evident, suggesting the presence of N doping in the carbon framework, although to a much lower extent compared to that of HP-N-CNF (Figure 3a). The deconvoluted C 1s spectrum shown in Figure S5b in the Supporting Information suggests three peaks centered at binding energies of 284.8, 286.1, and 288.6 eV, which correspond to the C=C, C—N, and C—O bonds, respectively, in the NP-N-CNF. However, the lower peak intensity of the C—N deconvoluted peak confirms that the N-doping extent is lower in NP-N-CNF than in HP-N-CNF. This result was further confirmed using quantification of nitrogen and carbon content, which were determined to be 3.9 and 76.7 wt%, respectively, using the EA technique, as shown in Table S1 in the Supporting Information. The Raman spectroscopy results shown in Figure S5c in the Supporting Information suggest a relatively high I_D/I_G value of ≈1.4 for NP-N-CNF, indicating that the carbonaceous material in the sample is mostly amorphous. Furthermore, the N_2 adsorption–desorption isotherms in Figure S5d in the Supporting Information reveal a low surface area of ≈8 m^2 g^{-1} (pore volume: 0.01 cm^3 g^{-1}) for the NP-N-CNF, thus indicating the absence of any pores. Overall, the above results signify that NP-N-CNF is mainly composed of amorphous nitrogen-doped carbonaceous material with a filled or dense-type morphology that envisage inferior electrochemical performance compared to HP-N-CNF.

To validate the structural merits of HP-N-CNF, the electrochemical performance of the Li—S cells was evaluated. For the same, free-standing electrodes were prepared by infiltrating the highly concentrated (0.95 M) LiPS catholyte as a sulfur source (Scheme 1⑤). For typical electrochemical measurements, the effective sulfur content and sulfur loading in the Li—S cells were fixed to 76.8 wt% and 4.8 mg cm^{-2}, respectively, with an E/S ratio of 9.6 µL mg^{-1}. The Li—S cell utilizing HP-N-CNF@LiPS electrodes was initially subjected to cyclic voltammetry (CV) tests at various scan rates ranging from 0.01 to 0.1 mV s^{-1} in the voltage window of 1.5–2.8 V. The CV profiles for initial four cycles at 0.01 mV s^{-1} are shown in **Figure 4**a, which exhibits slightly different electrochemical behavior during the initial two scans, as evident from the two well-separated cathodic peaks centered at 2.33 and 2.05 V during the reduction process. However, during the reverse anodic scan, two closely spaced peaks located at 2.32 and 2.38 V were observed for the first scan, which was shifted to a slightly higher potential during the second cycle to 2.38 and 2.40 V, respectively. The cathodic peak observed at 2.33 V is generally associated with the reduction of higher-order soluble LiPSs (Li_2S_n; $6 \le n \le 8$) to the middle-order LiPS (Li_2S_n; $4 \le n \le 6$).[5] Additionally, the

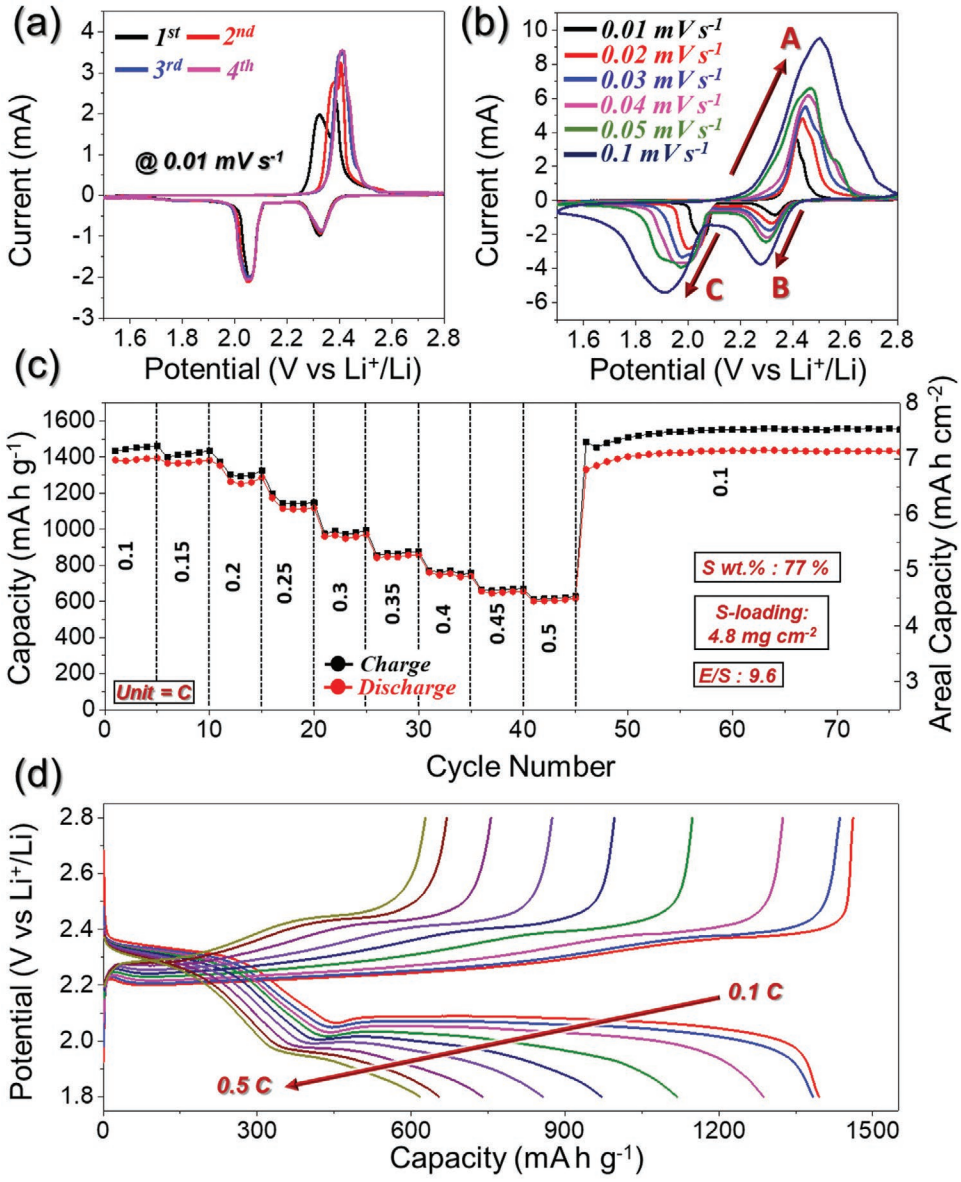

Figure 4. Electrochemical performance of the Li–S cells employing HP-N-CNF as free-standing cathode substrate and lithium polysulfide (Li_2S_6) catholyte as active material: a) cyclic voltammograms (CV) curves at 0.01 mV s^{-1} for four initial cycles, b) CV curves at different scan rates ranging from 0.01 to 0.1 mV s^{-1}, c) rate-capability test at various C-rates (0.1–0.5 C), and d) respective charge–discharge profiles of the Li–S cell for 5th cycle at different C-rates.

cathodic peak at 2.05 V is attributed to the continuous reduction of middle-order polysulfides to insoluble lower-order LiPSs (Li_2S_2/Li_2S).[5] During the oxidation scan, the lower-order polysulfides are first oxidized to higher-order LiPSs at 2.32 V via the middle-order polysulfides and then, are finally reduced to elemental sulfur at 2.38 V, thus completing the full redox process.[42–45] However, after the second cycle onward, the overlapping CV profiles suggest excellent reversibility of the redox process inside the Li–S cell. Furthermore, a similar shape profile even at a high scan rate of 0.1 mV s^{-1} suggests an identical electrochemical redox reaction inside the Li–S cell employing HP-N-CNF@LiPS electrode, as shown in Figure 4b. The above CV outcomes predict that the incorporation of HP-N-CNF as cathode substrate envisage outstanding electrochemical performance.

To further validate CV results, the Li–S cell employing an HP-N-CNF@LiPS electrode was subjected to the galvanostatic charge–discharge process in a stepwise manner at various current rates ranging from 0.1 to 0.5 C in the voltage window of 1.8–2.8 V. The current values corresponding to each C-rate were obtained by assuming a theoretical discharge capacity of 1675 mAh g^{-1}. The obtained rate capability results and respective charge–discharge profiles at different C-rates are shown in Figure 4c,d. The HP-N-CNF@LiPS electrode exhibits a discharge capacity of 1395, 1383, 1286, 1117, 971, 856, 739, 655, and 617 mAh g^{-1} for the 5th cycle at 0.1, 0.15, 0.2, 0.25, 0.3, 0.35,

0.4, 0.45, and 0.5 C, respectively. Moreover, when the current was reversed to 0.1 C-rate, the Li−S cell displayed a stable discharge capacity of 1428 mAh g^{-1} during continuous cycling. The obtained discharge capacities are particularly high, considering the high effective sulfur content of 76.8 wt% and high sulfur loading of 4.8 mg cm^{-2} in the Li−S cell combined with a low E/S ratio (9.6 µL mg^{-1}). In addition, the electrochemical results are comparable with those of previous reports, as displayed in Table S2 in the Supporting Information. Furthermore, the specific battery parameters agree well with the standard benchmarks set for the commercial applicability of the LSBs, i.e., a high active material content (>70 wt%), high sulfur loading (>4.0 mg cm^{-2}), and low E/S ratio (<11.0 µL mg^{-1}). Moreover, the corresponding areal capacity at various C-rates is either higher or comparable to the theoretical threshold of 4.0 mAh cm^{-2}. The remarkable rate performance of the Li−S cell could be attributed to the structural and morphological improvements that synergistically provide uniform dispersion and utilization of the active sulfur material in the form of LiPS catholyte. In addition, the high surface area in the form of numerous interconnected chain-like ordered mesopores provides enough space to absorb the severe volume variation originating from the density difference between elemental sulfur and its discharge product Li_2S. Moreover, the highly conductive N-C skeleton supports rapid ionic/electronic transport, which facilitates enhanced redox reactions. Overall, the combined strategy of introducing a highly porous and conductive nitrogen-doped carbon framework as a cathode substrate resulted in a significant rate capability with efficient active material utilization and enhanced capacity retention. The respective charge–discharge profiles for the 5th cycle at various C-rates shown in Figure 4d agree well with the CV results and further suggest a typical redox reaction between sulfur and Li_2S only via intermediate LiPSs, as evident from the well-resolved charge–discharge plateaus even at a high C-rate of 0.5 C. However, a marginally low discharge capacities compared to the charge capacities suggests slightly less concentration of Li ion that diffused into the cathode than diffused out during the charge. This is due to high viscosity of the catholyte which hindered the electronic contact between the carbon scaffold and the polysulfide species that subsequently decreases the Li ion diffusion.[46,47] Besides, the high discharge capacities of HP-N-CNF@LiPS electrode were further validated by considering the capacity utilization at different C-rates, as shown in Figure S6 in the Supporting Information. At a low C-rate of 0.1 C, the Li−S cell utilizes almost 83% of the active material, suggesting excellent reaction kinetics. Even at a high C-rate of 0.5 C, the active material utilization was ≈37%, indicating high active material participation in the electrochemical processes. Therefore, the above results suggest that the incorporation of HP-N-CNF as the cathode substrate for LSBs significantly enhanced the rate capability by improving the active material utilization during the redox reaction.

The cycling performance of the assembled typical Li−S cell (i.e., high sulfur content (76.8%), high sulfur loading (4.8 mg cm^{-2}), and low E/S ratio 9.6 µL mg^{-1}) utilizing the HP-N-CNF@LiPS electrode was also evaluated at different C-rates (0.1, 0.2, and 0.3 C), as shown in **Figure 5**. The assembled Li−S cell exhibited an initial discharge capacity of 1419 mAh g^{-1}, which is 85% of the theoretical value (1675 mAh g^{-1}) with an

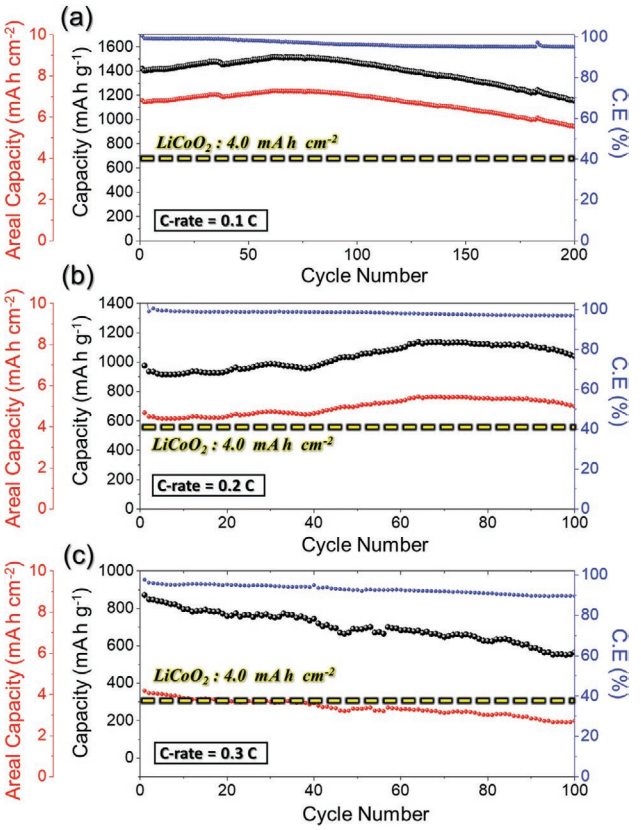

Figure 5. Cycling performance of the typical Li–S cells employing free-standing HP-N-CNF@LiPS electrode at different C-rates: a) 0.1 C, b) 0.2 C, and c) 0.3 C.

initial Coulombic efficiency of 100% at 0.1 C, as shown in Figure 5a. However, a monotonic increase in the discharge capacity up to 65 cycles was observed after a few initial cycles, which is attributed to the continuous activation of the active material.[48,49] The discharge capacity observed at the end of the 65th cycle was 1514 mAh g^{-1} (90% of the theoretical value). Afterward, the discharge capacity showed a decreasing trend with a value of 1334 mAh g^{-1} at the end of the 150th cycle (94% of the initial discharge capacity); however, upon further cycling, the discharge capacity was stabilized to 1155 mAh g^{-1} at the end of the 200th cycle with an average capacity decay of 0.18 mAh g^{-1} (0.93%) per cycle. The areal capacity is considered as a critical parameter to check the viability of Li−S cells and their ability to outperform commercially available Li ion arrangement ($LiCoO_2$IIgraphite system). The initial areal capacity of the Li−S cell employing the HP-N-CNF@LiPS cathode was ≈6.8 mAh cm^{-2}, which is 1.7 times higher than that of the commercial system (4.0 mAh cm^{-2}). Moreover, even after 200 cycles, the areal capacity (5.5 mAh cm^{-2}) value was well above the commercial standard, suggesting extraordinary reaction kinetics inside the Li−S cell. Likewise, high Coulombic efficiency of 95% after 200th cycles indicates the high reversibility of the redox reactions inside the Li−S cell. Furthermore, the charge–discharge profiles at various cycle numbers for 0.1 C are shown in Figure S7a in the Supporting Information, which suggests that even with practical parameters, the Li−S cell displays a typical charge–discharge mechanism inside the cell,

which results in high discharge capacities. In addition, the Li−S cell displays negligible voltage fading (0.02 mV per cycle) with an average discharge voltage of ≈2.1 V (Figure S7b, Supporting Information). These results clearly indicate that the structural advantages of HP-N-CNF resulted in a remarkable overall electrochemical performance. The assembled Li−S cells employing the sulfur electrode were further subjected to high C-rate cycling performance at 0.2 and 0.3 C, as shown in Figure 5b,c, respectively. The Li−S cells displayed initial discharge capacities of 976 and 871 mAh g^{-1} at 0.2 and 0.3 C, respectively. Upon further cycling, the Li−S cell cycled at 0.2 C displayed similar trends to 0.1 C cycling with a capacity increase until the 70th cycle and stabilized thereafter. In contrast, the Li–S cell cycled at 0.3 C (Figure 5c) displayed a slight capacity decay, which seems to be stabilized. The capacity decay is attributed to the marginally low anchoring of the polysulfide species, especially at higher C-rates. This eventually resulted in the formation of a passivation film on the surface of metallic lithium anode that increases the polarization over cycling and hence, capacity fading.[1] The discharge capacities at the end of the 100th cycle were 1040 and 565 mAh g^{-1} at 0.2 and 0.3 C, respectively, with Coulombic efficiencies of 97% and 89%. Furthermore, the areal capacity values of 5.0 and 2.7 mAh cm^{-2} at 0.2 and 0.3 C, respectively, at the end of the 100th cycle also appeared to be comparable with the theoretical benchmark of 4.0 mAh cm^{-2}. Moreover, it should be noted that the free-standing HP-N-CNF substrate contribute marginally to the total discharge capacity, as shown in Figure S8 in the Supporting Information.

To further explore the structural advantages of the HP-N-CNF cathode substrate as a free-standing sulfur electrode for developing viable LSBs, the electrochemical performance of the Li−S cells with extremely high areal loadings of the active material was investigated, as shown in **Figure 6**. The rate capability results obtained at various C-rates in a stepwise manner are shown in Figure 6a, along with the respective charge–discharge profiles for the 5th cycle in Figure 6b. The voltage window for Li−S cells with ultrahigh sulfur loadings was fixed from 1.5 to 2.8 V. The HP-N-CNF substrate infiltrated with lithium polysulfide catholyte to yield ultrahigh areal loading (10.0 mg cm^{-2}), and the high sulfur wt% (77.9%) electrode displayed initial discharge capacities of 575, 844, 676, 560, and 508 mAh g^{-1} at 0.05, 0.1, 0.15, 0.2, and 0.25 C, respectively. Moreover, when the current was reversed to 0.1 C, the Li−S cell retained 73% (618 mAh g^{-1}) of the initial discharge capacity at an identical C-rate. The rate capability results are impressive considering the very high sulfur loading/content and low E/S ratio (7.4 µL mg^{-1}). Moreover, the areal capacities at various C-rates still agreed well with the standard threshold. The respective charge–discharge profiles for the 5th cycle at various C-rates (Figure 6b) suggest typical redox reactions inside the cell with standard voltage plateaus. However, a slightly high discharge capacity value compared to the charge capacity especially at 0.05 C-rate is assigned to the side reactions of $LiNO_3$ reduction at voltages well below than 1.8 V, which can be clearly seen in the discharge voltage profile around the same voltage region.[50] Furthermore, the Li−S cells employing HP-N-CNF@LiPS free-standing cathode under such severe battery conditions were further subjected to cycling performance at 0.05 and 0.1 C-rate. The cycling results shown in Figure 6c,d indicate that the Li−S cells exhibit a discharge capacity of 1158 (2nd cycle) and 650 mAh g^{-1} (1st cycle) at 0.05 and 0.1 C-rate, respectively, which is 69% and 39% of the theoretical discharge capacity. Upon further cycling, the Li−S cell cycled at 0.05 C displays monotonic capacity decay until the 45th cycle with a discharge capacity of 798 mAh g^{-1} (69% of the 2nd cycle) and seems to stabilize thereafter. At the end of the 100th cycle, the cell exhibited a stable discharge capacity of 621 mAh g^{-1} (54% of the 2nd cycle). Likewise, the Li−S cell cycled at 0.1 C-rate displayed a maximum discharge capacity of 900 mAh g^{-1} at the end of the 39th cycle owing to the activation process of the starting material.[49] With continuous cycling, the cell displayed a stable discharge capacity of 389 mAh g^{-1} at the end of the 200th cycle. Furthermore, the Li–S cells cycled at 0.05 and 0.1 C displayed an average capacity decay of 0.21% and 0.20% per cycle, respectively, which is reasonable considering the severe battery conditions. Moreover, the high Coulombic efficiency values throughout the cycles indicate a reversible electrochemical process inside the cell. Furthermore, the high and stable areal capacity of ≈6.2 and 4.0 mAh cm^{-2} at 0.05 and 0.1 C, respectively, confirm the feasibility of the HP-N-CNF free-standing electrode for commercial applications. These results clearly suggest that the structural merits of the HP-N-CNF cathode substrate resulted in more practical battery performance, even with the strident battery parameters.

Furthermore, a Li–S cell employing the HP-N-CNF cathode substrate with extremely high sulfur content (83.2 wt%) and loading (14.3 mg cm^{-2}) was also assembled to further exploit the structural advantages and subjected to cyclic performance at 0.05 C-rate, as shown in **Figure 7**a. The Li–S cell displayed an initial discharge capacity of 450 mAh g^{-1}, which steadily increased to 858 mAh g^{-1} at the 12th cycle, which was attributed to the activation process.[48] Subsequently, the discharge capacity decreased and tended to stabilize after 130 continuous charge–discharge cycles at 383 mAh g^{-1}. Moreover, the Li–S cell displayed capacity retention of 85% with an average capacity decay rate of 0.11% per cycle. Besides, the cell exhibited a high Coulombic efficiency of 89% at the end of the 130th cycle, suggesting highly reversible electrochemical processes inside the cell. Furthermore, the assembled cell displayed an initial areal capacity of 6.4 mAh cm^{-2} which further increased to 12.2 mAh cm^{-2} at the end of the 12th cycle and finally stabilized at ≈5.5 mAh cm^{-2} after the 130th cycle, which is again much higher than the theoretical threshold of 4.0 mAh cm^{-2} for the presently available commercial system. Notably, the E/S ratio inside the cell is only 6.8 µL mg^{-1} (total electrolyte volume is 150 µL). The electrochemical performance obtained in the present work is summarized and compared with previously reported cathode substrates employing polysulfide catholyte as a sulfur source, as shown in Table S2 in the Supporting Information and Figure 7b,c. The comparative analysis clearly suggests that the structural merits of the HP-N-CNF substrate result in viable LSBs with remarkable electrochemical performance, which are either superior or comparable to those reported in previous studies. Moreover, the respective charge–discharge profiles at various cycle numbers displayed in Figure S9 in the Supporting Information suggest typical electrochemical redox reactions inside the Li–S cell even at ultrahigh sulfur content. Furthermore, the Li–S cells with different sulfur loading

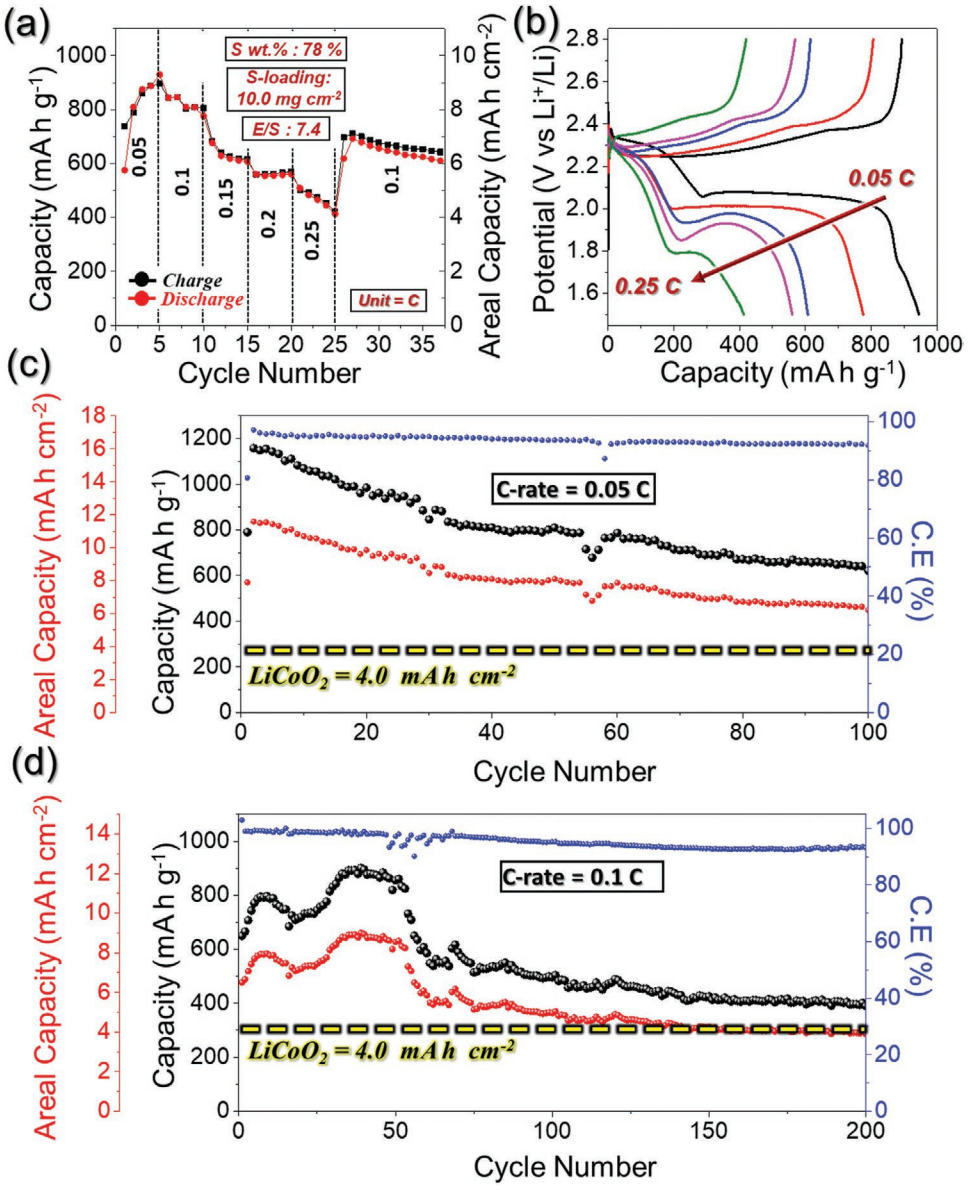

Figure 6. Electrochemical performance of the Li–S cells employing free-standing HP-N-CNF@LiPS electrode with high active material loading (10.0 mg cm^{-2}): a) rate capability test, b) respective charge–discharge profile for 5th cycle at different C-rates, and c,d) cycling performance at 0.05 and 0.1 C-rate, respectively. The E/S ratio value inside the Li–S cells was fixed to 7.4 µL mg^{-1} for the above electrochemical tests.

of 10.0 and 14.3 mg cm^{-2} were connected in series to power an external load (a 5 V, 10 mW light-emitting diode) after cycling at 0.05 C-rate, as shown in Figure 7d. The series combination provides an uninterrupted power supply to the load continuously for 20 m and thus authenticates all the electrochemical results obtained above. Moreover, high gravimetric energy density calculated at both cell and electrode level along with the volumetric energy density for Li–S cells utilizing different sulfur loading (Table S3, Supporting Information) again indicates the practical application potential of this strategy.

To confirm the structural superiority of the HP-N-CNF, pristine nonporous NP-N-CNF prepared using the spinning solution without ZIF-8 polyhedra were also tested in a Li–S cell configuration. However, the amount of lithium polysulfide catholyte was restricted to 20 µL only compared to 40 µL for the HP-N-CNF cathode substrate owing to the dense morphology of the nanofibers, which makes it difficult to absorb the excessive volume of highly concentrated polysulfide. Thus, the effective sulfur content and loading in the NP-N-CNF electrode (∅ = 14 mm) were 34.9 wt% (electrode wt. = 6.8 mg) and 2.38 mg cm^{-2}, respectively. The electrolyte volume inside all the Li–S cells was fixed at 30 µL. The CV curves for the initial four cycles at a scan rate of 0.01 mV s^{-1} in the voltage window of 1.8–2.8 V are shown in Figure S10a in the Supporting Information. Even at a low sulfur content and low loading, the CV curves displayed somewhat incomplete redox reactions, as can be observed from the single cathodic peak at 2.19 V and broad anodic peak centered at 2.57 V. Furthermore, the high

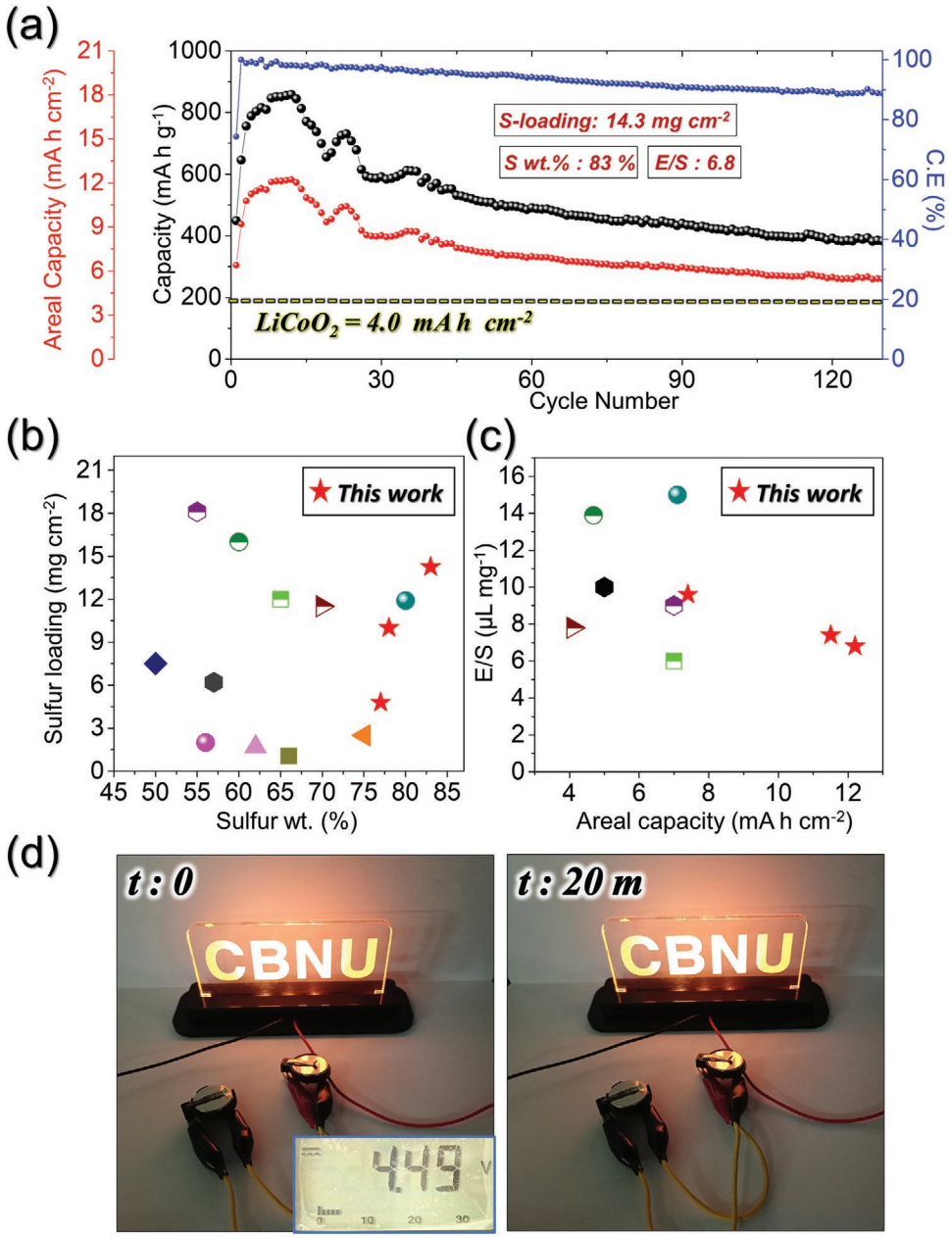

Figure 7. Electrochemical performance of the Li–S cell with strident battery parameters such as super-high sulfur content (83.0 wt%), ultrahigh loading (14.3 mg cm^{-2}), and low E/S ratio (6.8 µL mg^{-1}): a) cycling performance at 0.05 C-rate, b,c) comparison of various battery parameters obtained in the present work with the previously reported works, and d) digital photographs of a light-emitting diode (5 V, 10 mW) powered by series combination of two Li–S cells with sulfur loadings of 10.0 and 14.3 mg cm^{-2} after cycling at 0.05 C-rate.

polarization potential (ΔV = 0.38 V compared to 0.27 V for HP-N-CNF) and low current values suggest sluggish redox reactions inside the cell. The CV profiles corresponding to various scan rates ranging from 0.01 to 0.1 mV s^{-1} are shown in Figure S10b in the Supporting Information. With an increase in scan rate, the polarization potential also increases, suggesting inferior reaction processes. To authenticate the CV results, the Li–S cell employing the NP-N-CNF@LiPS electrode was subjected to a rate performance test in a stepwise manner at various C-rates ranging from 0.1 to 0.5 C in the voltage window of 1.8–2.8 V, as shown in Figure S10c in the Supporting Information. The assembled cell displayed initial discharge capacities of 156, 85, 32, and 5 mAh g^{-1} for the 5th cycle at 0.1, 0.15, 0.2, and 0.25 C-rate, respectively. However, after 0.25 C, the cell displayed almost zero discharge capacity, thus verifying the CV results. Furthermore, when the current was reversed to 0.1 C, the Li–S cell exhibited a stable discharge capacity of ≈159 mAh g^{-1} with continuous cycling, although the capacity was poor compared to that of HP-N-CNF. The respective charge–discharge profiles at various C-rates are shown in Figure S10d in the Supporting Information, which clearly indicates the absence of typical charge–discharge voltage plateaus, which

subsequently resulted in low discharge capacity values. Furthermore, the cycling performance of the Li–S cell utilizing the NP-N-CNF cathode substrate at various C-rates (0.1, 0.2, and 0.3 C) is shown in Figure S11 in the Supporting Information. Even at a low C-rate of 0.1 C, the assembled Li–S cell exhibited a low discharge capacity (≈79 mAh g^{-1} for the initial cycle) and poor capacity retention (53% after 200 cycles). In addition, at high C-rates, the cells displayed almost zero discharge capacities. The cycling result further confirms that even at minimal effective sulfur content or sulfur loading and high E/S ratio (13.7 µL mg^{-1}), Li–S cells with NP-N-CNF@LiPS cathode display inferior electrochemical performance.

The exceptional electrochemical performance of the HP-N-CNF@LiPS electrode was verified by electrochemical impedance spectroscopy measurements of the Li–S cells before and after cycling at 0.2 C in a fully lithiated state, as shown in Figure S12 in the Supporting Information. The similar solution resistance (R_s) value (≈8.0 Ω) in the Li–S cell employing the HP-N-CNF electrode before and after cycling suggests similar electrode–electrolyte interface interactions. However, a decrease in the charge resistance (R_{ct}) value from 60.0 to 32.0 Ω (Figure S12a, Supporting Information) after cycling at the 0.2 C-rate suggests enhanced reaction kinetics inside the cell. In contrast, the Li–S cell utilizing pristine NP-N-CNF displayed very high R_{ct} values (≈1050 Ω) before and after cycling (Figure S12b, Supporting Information), indicating a sluggish redox reaction inside the cell. These results again validate the structural superiority of the free-standing HP-N-CNF cathode substrate for feasible LSBs.

To authenticate the structural advantages and remarkable electrochemical performance of HP-N-CNF, electrocatalytic activity, and adsorption tests were performed, as shown in Figure S13 in the Supporting Information. For electrocatalytic activity tests, the CV curves (Figure S13a, Supporting Information) were obtained using symmetric cells in the voltage window of –1.0 to 1.0 V at a scan rate of 3 mV s^{-1}, in which HP-N-CNF and NP-N-CNF were utilized as both the counter and working electrodes. The CV curves shown in Figure S13a in the Supporting Information clearly indicate that the HP-N-CNF cathode substrate displays well-resolved redox peaks at 0.26 and –0.30 V with appreciable current values compared to the NP-N-CNF substrate that exhibits a nearly flat CV profile. The well-separated and high current redox peaks for HP-N-CNF indicate efficient electrocatalytic activity for polysulfide conversion. The CV results for symmetric cells were further strengthened by analyzing the results of the visual polysulfide adsorption tests to demonstrate the interaction between the polysulfides and prepared free-standing substrates, as shown in Figure S13b–d in the Supporting Information. Three glass vials were filled with 1.0×10^{-3} M of Li_2S_6 polysulfide solution in a suitable amount of 1,3-dioxolane (DOL)/1,2-dimethoxyethane (DME) (1:1 v/v) solvent, as shown in Figure S13b in the Supporting Information. Thereafter, 3.0 mg of HP-N-CNF and NP-N-CNF samples were added to the vials, stirred inside the glove box for 10 min, and allowed to settle afterward. Figure S13c,d in the Supporting Information show the digital photographs of the three vials immediately after stirring (represented by $t = 0$) and after 20 min. As shown in Figure S13b,d in the Supporting Information, a clear color change from brown to nearly transparent for HP-N-CNF suggests effective polysulfide anchoring compared to the NP-N-CNF, which still displays yellowish color of the polysulfide solution (Figure S13d, Supporting Information), indicating poor polysulfide adsorption capability. These results confirm that the structural merits of HP-N-CNF resulted in efficient mitigation of polysulfide migration toward the anode, which subsequently resulted in high active material utilization and, therefore, improved the overall electrochemical performance.

Postcycling characterizations such as FE-SEM and elemental dot mapping were performed for the Li–S cells employing HP-N-CNF@LiPS and NP-N-CNF@LiPS electrodes to evaluate the possible causes for the differences in the electrochemical performance. The Li–S cells were opened inside the glovebox after cycling for 100 cycles at 0.2 C-rate followed by careful removal of the free-standing electrodes and subsequent drying to evaporate the solvents. The FE-SEM micrographs of the HP-N-CNF@LiPS cycled electrode (Figure S14a, Supporting Information) recovered after the 100th cycle at the 0.2 C-rate reveals that the 1D nanofiber morphology remained intact even after cycling. However, it can be clearly observed that the highly porous fibrous structure was filled with liquid catholyte. In contrast, the FE-SEM images of the cycled NP-N-CNF@LiPS electrode (Figure S14b, Supporting Information) suggest that most of the polysulfide catholyte volume was unabsorbed owing to the dense morphology of the NP-N-CNF, which subsequently resulted in a high percentage of the unutilized active material and, therefore, substandard electrochemical performance. These results indicate that the porous nanostructure in the HP-N-CNF cathode substrate that arises from the interconnected chain-like hollow N-C nanocages provides enough space not only to absorb the high volume of liquid catholyte completely but also channelize the severe volume variation of the active material over continuous cycling within the nanofiber domain so that it can be utilized repeatedly, thus providing exceptional electrochemical kinetics. The postcycling digital photographs of the Celgard separator facing the lithium anode are shown in Figure S14c,d in the Supporting Information, which are consistent with the FE-SEM results. The lithium polysulfide deposits can be clearly observed on the surface of Celgard (Figure S14d, Supporting Information), suggesting poor polysulfide anchoring by NP-N-CNF. In contrast, no such deposits were observed on the Celgard surface recovered from the Li–S cell employing the HP-N-CNF electrode. However, the slightly blackish deposits are believed to be from the free-standing HP-N-CNF substrate, which remains on the separator surface while separating it from the electrode. In addition, the separator recovered from the cell employing the NP-N-CNF@LiPS electrode displayed a severe color change to yellow, even if the cathode substrate was infiltrated with low effective sulfur content and low loading, thus indicating a high concentration of dissolved lithium polysulfides on the lithium side. In contrast, the separator recovered from the cell employing the HP-N-CNF@LiPS electrode displays a slight color change to light brown, suggesting efficient mitigation of polysulfide diffusion toward the lithium anode and, therefore, minimum active material loss. These results are well supported by the elemental dot mapping FE-SEM images of the anode facing side of cycled electrodes, as shown in Figure S15a,b in

the Supporting Information. The high sulfur deposits can be clearly seen for the NP-N-CNF@LiPS electrode with a high sulfur content (14.7%), whereas HP-N-CNF@LiPS displays a uniform dispersion of sulfur species in the carbon framework with no obvious polysulfide deposits, resulting in high sulfur utilization, as evident from the low sulfur percentage (13.0%). In addition, the structural changes in the cycled anode along with the sulfur content were analyzed using FE-SEM and energy dispersive spectroscopy (EDS) mapping, as shown in Figure S16 in the Supporting Information. The lithium surface displays less sulfur deposits (Figure S16a, Supporting Information) for cell utilizing HP-N-CNF substrate compared to the cell with NP-N-CNF substrate (Figure S16c, Supporting Information), suggesting better sulfur immobilization and therefore, low active material loss. This observation is well supported by the EDS mapping results for sulfur element in Figure S16b in the Supporting Information. Even with a low sulfur content and low active material loading for cell using NP-N-CNF substrate, sulfur species diffuse toward lithium anode in high percentage that eventually results in severe parasitic reactions along with inferior electrochemical performance due to high active material loss. These results clearly suggest that the structural merits of the HP-N-CNF cathode substrate resulted in remarkable electrochemical performance. Furthermore, post-cycling thickness measurement was also performed to analyze the expansion tolerant capabilities of the free-standing HP-N-CNF cathode substrate (Figure S17, Supporting Information). The structural integrity of the free-standing electrode was again evident (Figure S17a, Supporting Information), which reveals a crack free electrode even with feasible battery parameters. Besides, the volume expansion (which arises due to the density difference between the elemental S and its discharge product Li_2S) tolerant capability was also confirmed in Figure S17b in the Supporting Information, indicating that the thickness of electrode increases to 535 μm (compared to 383 μm for uncycled substrate (Figure S1c, Supporting Information)). This indicates that even with a thickness expansion of 40%, the electrode maintains high mechanical integrity, which clearly justifies the overwhelming electrochemical performance.

Overall, the rational design strategy used for the synthesis of highly porous nitrogen-doped carbon nanofibers resulted in a suitable cathode substrate that could not only withstand the acute battery parameters but also provide exceptional electrochemical performance. We believe that the comprehensive approach used in this work for sustainable LSBs with more practical conditions could provide extensive knowledge for the development of more advanced cathode substrates as host materials.

3. Conclusions

In summary, we utilized a highly porous N-doped C nanofiber cathode substrate comprising tightly packed interconnected chain-like hollow N-C nanocages with open pores as a sulfur host material to produce highly sustainable LSBs with strident battery parameters. The highly porous nanostructure not only allows efficient encapsulation of a high volume of active material but also provides enough space to absorb the severe volume changes during the electrochemical processes, along with efficient electrolyte percolation that allows smooth diffusion of conductive species. In addition, the highly conductive N-doped C skeleton with numerous conductive pathways allows fast ionic/electronic transfer for kinetically favored redox reactions. Benefiting from such uniquely designed conductive and porous nanostructures, high active material utilization and efficient polysulfide anchoring were achieved. Thus, the LSBs utilizing the HP-N-CNF cathode substrate resulted in exceptional electrochemical performance with practical battery parameters such as super-high sulfur content (83.2 wt%), ultrahigh sulfur loading (14.3 mg cm^{-2}), and low E/S ratio (6.8 μL mg^{-1}). Therefore, we surmise that the morphological and electrochemical advancements presented in this work could provide substantial knowledge for the development of high-energy-density metal–sulfur battery systems.

4. Experimental Section

Chemicals: All chemicals used for synthesizing highly porous nitrogen-doped carbon nanofibers were of analytical grade: PAN (M_w = 150 000, Sigma-Aldrich), zinc nitrate hexahydrate ($Zn(NO_3)_2{\cdot}6H_2O$; M_w = 297.47, 96%, Samchun Chemicals), and 2-methylimidazole (M_w = 82.10, 99%, Acros Organics). The spinning solution was prepared in *N,N*-dimethylformamide (DMF, 99.5%, Samchun Chemicals) as the solvent.

Sample Preparation: HP-N-CNFs were synthesized using the conventional electrospinning technique followed by one-step carbonization. First, a PAN/ZIF-8 composite nanofiber mat was obtained by electrospinning and subsequent stabilization. Ultrafine ZIF-8 polyhedra (∅ = 100 nm) were synthesized. Briefly, a stoichiometric amount of $Zn(NO_3)_2{\cdot}6H_2O$ was added to methanol as the solvent. Another solution of 2-methylimidazole in methanol was also prepared and added to the above solution. Finally, the colloidal suspension was centrifuged, washed repeatedly, and dried in air to obtain uniform-sized ZIF-8 polyhedra.[3] To obtain a spinning solution, 3.0 g of the as-prepared ZIF-8 polyhedra was dispersed in 20 mL of DMF solution and stirred for 2 h followed by ultrasonication for another 1 h. Subsequently, 1.5 g of PAN was added slowly to the milky ZIF-8/DMF solution and stirred overnight for homogeneous mixing. The obtained spinning solution was loaded into a plastic syringe pump (12 mL capacity) fitted with a 21-gauge stainless-steel needle. The flow rate of the spinning solution was fixed at 2 mL h^{-1}, whereas the voltage between the needle and the rotating drum collector (covered with the Al foil) was set at 20 kV. The distance between the collector and tip was fixed at 15 cm throughout the spinning process. The as-spun PAN/ZIF-8 composite nanofibers were stabilized at 150 °C overnight in a hot-air oven. The stabilized PAN/ZIF-8 nanofibers were then subjected to a single-step heat-treatment process at 1000 °C for 2 h in a N_2 atmosphere to obtain HP-N-CNFs. For comparison, nonporous nitrogen-doped carbon nanofibers (NP-N-CNFs), i.e., without ZIF-8 polyhedra, were prepared using identical electrospinning conditions. However, the as-spun PAN nanofibers were stabilized first at 150 °C overnight and then at 200 °C for 1 h in air, followed by carbonization at 400 °C for 5 h in a N_2 atmosphere.

Physical Characterization Techniques: Morphological analysis of the as-prepared HP-N-CNF was carried out using a FE-SEM (Ultra Plus, Zeiss) and field-emission transmission electron microscopy (FE-TEM; JEM-2100F, JEOL). The crystal structure and phase purity of the nanofibers were observed using XRD (Bruker, D8 Discover) equipped with Cu $K_{\alpha 1}$ radiation (1.5405 Å) at the Korea Basic Science Institute (Daegu). The thermal stability of the nanofibers was studied using TGA (Pyris 1, Perkin Elmer) in the temperature range of 25–1000 °C at a heating rate of 10 °C min^{-1} in a N_2 atmosphere or mentioned otherwise. An XPS (K-Alpha, Thermo Scientific) instrument with Al K_α radiation was used to observe the chemical composition of all elements in the prepared

nanofibers. The surface area and pore volume of the nanofibers were measured using the BET technique using N_2 adsorption–desorption isotherms. The quantification of carbon and nitrogen content in the nanofibers was performed using EA technique. The structural properties of the carbonaceous material in the nanofibers were measured using Raman spectroscopy (LabRam, HR800, Horiba Jobin-Yvon) technique.

Catholyte Preparation: To prepare the LiPS catholyte blend, stoichiometric amounts of elemental sulfur (S, M_w = 32.07, Sigma-Aldrich, 99.98%) and lithium sulfide (Li_2S; M_w = 45.95, Sigma-Aldrich, 99.98%) were mixed in a 1:5 weight ratio in the bare electrolyte to obtain Li_2S_6 (Equation (1)). The electrolyte used was a 1.0 mol L^{-1} solution of lithium bis-(trifluoromethanesulfonyl) imide in a mixture of DOL and DME (1:1 v/v) with 0.5 mol L^{-1} $LiNO_3$ as an additive. The S and Li_2S mixtures in the bare electrolyte solution were stirred overnight inside a glove box at 70 °C to form a highly concentrated active material (5.7 M) in the form of a LiPS solution (0.95 M). Finally, a dark brown LiPS solution was obtained and used as the catholyte for electrochemical measurements. It should be noted that the concentration of the blends was calculated in terms of total atomic sulfur (referred to worked example in the Supporting Information). For, e.g., a 0.95 M of Li_2S_6 resulted in a sulfur concentration of 5.7 M as Li_2S_6 contains six sulfur atoms (6 × 0.95 M = 5.7 M).

$$Li_2S + \frac{(n-1)}{8}S_8 \rightarrow Li_2S_n \quad (1)$$

Cell Assembly and Electrochemical Measurements: To perform electrochemical measurements, CR2032 coin cells were assembled inside a glove box using free-standing HP-N-CNF@LiPS as cathode, lithium metal as an anode, and polypropylene Celgard as a separator. For typical electrochemical measurements, free-standing HP-N-CNF circular electrodes (∅ = 14 mm, average weight = 2.2 mg, and thickness = 383 µm; Figure S1, Supporting Information) were infiltrated with 40 µL of 0.95 M Li_2S_6 polysulfide catholyte solution. This resulted in a sulfur loading of ≈4.8 mg cm^{-2} with an ultrahigh effective sulfur content of ≈76.8 wt%. For viable electrochemical performance, the sulfur loading inside the Li–S cells was further increased to ≈10.0 (77.9 wt%) and 14.3 mg cm^{-2} (83.2 wt%), respectively. The amount of catholyte used for such a super-high loading arrangement was 85 and 120 µL, respectively, whereas the weight of the cathode substrate was fixed to 4.4 mg. The effective sulfur weight percentage was calculated by dividing the weight of sulfur in the form of a catholyte by the total weight of the HP-N-CNF electrode and sulfur. The volume of electrolyte used during the electrochemical measurements was fixed at 30 µL. The E/S value inside the assembled cells was calculated based on the total volume of bare electrolyte and the catholyte which comes out to be 9.6, 7.4, and 6.8 µL mg^{-1} for sulfur loading of 4.8, 10.0, and 14.3 mg cm^{-2}, respectively. The assembled Li–S cells were analyzed for various electrochemical characteristics using a WBCS3000 battery cycler (WonATech). The rate capability tests were carried out at various C-rates in the voltage window of 1.8–2.8 V for typical loading Li–S cells, whereas for high loading electrodes, a voltage range of 1.5–2.8 V was used. The current values corresponding to various C-rates were calculated by assuming a theoretical discharge capacity value of 1C = 1675 mAh g^{-1}. CV measurements were carried out at different voltage sweeping rates ranging from 0.01 to 0.1 mV s^{-1}. Nyquist plot measurements of the Li–S cells were performed using an impedance analyzer (ZIVESP2 Electrochemical workstation) in the frequency range of 100 kHz to 10 mHz with an alternating current (AC) pulse with an amplitude of 5 mV. The cycling performance was also evaluated at various C-rates for the typical and high-loading electrodes.

Electrocatalytic Activity and Polysulfide Tests: The efficient anchoring of LiPS inside the Li–S cell was observed using a symmetric cell configuration. Visual polysulfide adsorption tests were also performed using the LiPS solution and prepared samples. For these studies, a 2.0 M sulfur solution in the form of the Li_2S_6 catholyte was prepared in the DOL/DME solvent containing 1.0 mol L^{-1} LiTFSI salt. For symmetric cell assembly, the prepared HP-N-CNF and NP-N-CNF samples were mixed with carbon black and polyvinylidene fluoride binder in a weight ratio of 8:1:1 and dispersed in a minimum volume of *N*-methyl-2-pyrrolidone solvent, followed by slurry casting onto an aluminum foil. The symmetric cells were assembled using HP-N-CNF and NP-N-CNF electrodes (∅ = 14 mm) as counter and working electrodes separated by a Celgard 2400 membrane with the addition of 10 µL polysulfide solution. The CV tests for symmetric cells were carried out in the voltage window of –1.0 to 1.0 V at a scan rate of 3.0 mV s^{-1}. For the polysulfide adsorption tests, two glass vials containing the prepared sample were loaded with LiPS solution (1.0×10^{-3} M of Li_2S_6 in a suitable amount of DOL/DME) and stirred inside the glove box. A standard blank polysulfide solution was prepared for comparison.

Supporting Information

Supporting Information is available from the Wiley Online Library or from the author.

Acknowledgements

This work was supported by a National Research Foundation of Korea (NRF) grant funded by the Korean Government (MSIP) (NRF-2021R1A4A2001687 and NRF-2021R1I1A3057700).

Conflict of Interest

The authors declare no conflict of interest.

Data Availability Statement

The data that support the findings of this study are available in the Supporting Information of this article.

Keywords

feasible lithium–sulfur batteries, free-standing sulfur hosts, metal–organic frameworks, nitrogen-doped carbon, porous materials

Received: January 12, 2022
Revised: February 15, 2022
Published online:

[1] L. Qie, C. Zu, A. Manthiram, *Adv. Energy Mater.* **2016**, *6*, 1502459.
[2] L. Luo, S. H. Chung, A. Manthiram, *Adv. Energy Mater.* **2018**, *8*, 1801014.
[3] R. Saroha, J. H. Oh, Y. H. Seon, Y. C. Kang, J. S. Lee, J. S. Cho, *J. Mater. Chem. A* **2021**, *9*, 11651.
[4] R. Saroha, J.-H. Ahn, J. S. Cho, *Korean J. Chem. Eng.* **2021**, *38*, 461.
[5] R. Saroha, J. H. Oh, J. S. Lee, Y. C. Kang, S. M. Jeong, D.-W. Kang, C. Cho, J. S. Cho, *Chem. Eng. J.* **2021**, *426*, 130805.
[6] J. Wang, K. Xiao, B. Ouyang, L. Zhang, H. Yang, J. Liu, P. Liang, R. S. Rawat, Z. Shen, *ACS Appl. Energy Mater.* **2019**, *2*, 2570.
[7] L. Zhou, H. Li, X. Wu, Y. Zhang, D. L. Danilov, R. d.-A. Eichel, P. H. Notten, *ACS Appl. Energy Mater.* **2019**, *2*, 8153.
[8] S. Bai, X. Liu, K. Zhu, S. Wu, H. Zhou, *Nat. Energy* **2016**, *1*, 16094.
[9] S.-H. Yeon, W. Ahn, K.-H. Shin, C.-S. Jin, K.-N. Jung, J.-D. Jeon, S. Lim, Y. Kim, *Korean J. Chem. Eng.* **2015**, *32*, 867.
[10] R. Saroha, J. Heo, Y. Liu, N. Angulakshmi, Y. Lee, K.-K. Cho, H.-J. Ahn, J.-H. Ahn, *Chem. Eng. J.* **2022**, *431*, 134205.

[11] R. Liu, F. Guo, X. Zhang, J. Yang, M. Li, W. Miaomiao, H. Liu, M. Feng, L. Zhang, *ACS Appl. Energy Mater.* **2019**, *2*, 1348.
[12] S.-H. Chung, L. Luo, A. Manthiram, *ACS Energy Lett.* **2018**, *3*, 568.
[13] H. J. Peng, J. Q. Huang, X. B. Cheng, Q. Zhang, *Adv. Energy Mater.* **2017**, *7*, 1700260.
[14] Z. Wang, B. Wang, Y. Yang, Y. Cui, Z. Wang, B. Chen, G. Qian, *ACS Appl. Mater. Interfaces* **2015**, *7*, 20999.
[15] C. Ye, L. Zhang, C. Guo, D. Li, A. Vasileff, H. Wang, S. Z. Qiao, *Adv. Funct. Mater.* **2017**, *27*, 1702524.
[16] P. Chiochan, S. Kosasang, N. Ma, S. Duangdangchote, P. Suktha, M. Sawangphruk, *Carbon* **2020**, *158*, 244.
[17] P. G. Bruce, S. A. Freunberger, L. J. Hardwick, J.-M. Tarascon, *Nat. Mater.* **2012**, *11*, 19.
[18] S. Lu, Y. Chen, X. Wu, Z. Wang, Y. Li, *Sci. Rep.* **2014**, *4*, 4629.
[19] S. H. Chung, A. Manthiram, *Adv. Mater.* **2018**, *30*, 1705951.
[20] R. Yu, S.-H. Chung, C.-H. Chen, A. Manthiram, *Energy Storage Mater.* **2019**, *18*, 491.
[21] Z.-L. Xu, J.-K. Kim, K. Kang, *Nano Today* **2018**, *19*, 84.
[22] C.-H. Chang, S.-H. Chung, *Mater. Horiz.* **2017**, *4*, 249.
[23] R. Fang, S. Zhao, P. Hou, M. Cheng, S. Wang, H. M. Cheng, C. Liu, F. Li, *Adv. Mater.* **2016**, *28*, 3374.
[24] S.-H. Chung, C.-H. Chang, *ACS Nano* **2016**, *10*, 10462.
[25] L. Luo, S.-H. Chung, A. Manthiram, *J. Mater. Chem. A* **2018**, *6*, 7659.
[26] H. Xu, A. Manthiram, *Nano Energy* **2017**, *33*, 124.
[27] Y. Mao, G. Li, Y. Guo, Z. Li, C. Liang, X. Peng, Z. Lin, *Nat. Commun.* **2017**, *8*, 14628.
[28] S. Yao, S. Xue, S. Peng, M. Jing, X. Shen, T. Li, Z. YiLiu, *Int. J. Energy Res.* **2019**, *43*, 1892.
[29] X. Guo, K. Li, W. Bao, Y. Zhao, J. Xu, H. Liu, G. Wang, *Energy Technol.* **2018**, *6*, 251.
[30] L. Qie, A. Manthiram, *Adv. Mater.* **2015**, *27*, 1694.
[31] E. Lim, J. Chun, C. Jo, J. Hwang, *Korean J. Chem. Eng.* **2021**, *38*, 227.
[32] L. Fan, P. Sun, L. Yang, Z. Xu, *Korean J. Chem. Eng.* **2020**, *37*, 166.
[33] S. Ghosh, W. D. Yong, E. M. Jin, S. R. Polaki, S. M. Jeong, H. Jun, *Korean J. Chem. Eng.* **2019**, *36*, 312.
[34] S.-K. Park, J.-S. Park, Y. C. Kang, *J. Mater. Chem. A* **2018**, *6*, 1028.
[35] X. Song, Y. Jiang, F. Cheng, J. Earnshaw, J. Na, X. Li, Y. Yamauchi, *Small* **2021**, *17*, 2004142.
[36] M. S. Jo, J. S. Lee, S. Y. Jeong, J. K. Kim, Y. C. Kang, D. W. Kang, S. M. Jeong, J. S. Cho, *Small* **2020**, *16*, 2003391.
[37] J. S. Lee, M. S. Jo, R. Saroha, D. S. Jung, Y. H. Seon, J. S. Lee, Y. C. Kang, D. W. Kang, J. S. Cho, *Small* **2020**, *16*, 2002213.
[38] R. Saroha, A. K. Panwar, *J. Phys. D: Appl. Phys.* **2017**, *50*, 255501.
[39] H.-Y. Liu, L. Xu, Q.-L. Sun, *Therm. Sci.* **2015**, *19*, 1357.
[40] S. Kim, Y. S. Chung, H.-S. Choi, F.-L. Jin, S.-J. Park, *Bull. Korean Chem. Soc.* **2013**, *34*, 3733.
[41] Y. Ge, Z. Fu, Y. Deng, M. Zhang, H. Zhang, *J. Mater. Sci.* **2019**, *54*, 12592.
[42] B. Moorthy, S. Kwon, J.-H. Kim, P. Ragupathy, H. M. Lee, D. K. Kim, *Nanoscale Horiz.* **2019**, *4*, 214.
[43] L. Qu, P. Liu, Y. Yi, T. Wang, P. Yang, X. Tian, M. Li, B. Yang, S. Dai, *ChemSusChem* **2019**, *12*, 213.
[44] C. Deng, Z. Wang, S. Wang, J. Yu, D. J. Martin, A. K. Nanjundan, Y. Yamauchi, *ACS Appl. Mater. Interfaces* **2018**, *11*, 541.
[45] A. Gupta, A. Manthiram, *J. Mater. Chem. A* **2021**, *9*, 13242.
[46] S. Drvarič Talian, J. Bobnar, J. Moškon, R. Dominko, M. Gaberšček, *Electrochim. Acta* **2020**, *354*, 136696.
[47] J. Yan, X. Liu, B. Li, *Adv. Sci.* **2016**, *3*, 1600101.
[48] K. Sun, H. Liu, H. Gan, *Energy Convers. Storage* **2016**, *13*, 021002.
[49] C. Luo, E. Hu, K. J. Gaskell, X. Fan, T. Gao, C. Cui, S. Ghose, X.-Q. Yang, C. Wang, *Proc. Natl. Acad. Sci. USA* **2020**, *117*, 14712.
[50] N. Ding, L. Zhou, C. Zhou, D. Geng, J. Yang, S. W. Chien, Z. Liu, M.-F. Ng, A. Yu, T. A. Hor, *Sci. Rep.* **2016**, *6*, 33154.